

Deriving surface ultraviolet radiation from CERES surface and atmospheric radiation budget: Methodology

Wenying Su

Center for Atmospheric Sciences, Hampton University, Hampton, Virginia, USA

Thomas P. Charlock

NASA Langley Research Center, Hampton, Virginia, USA

Fred G. Rose

Analytical Services and Materials, Inc., Hampton, Virginia, USA

Received 24 January 2005; revised 4 April 2005; accepted 28 April 2005; published 30 July 2005.

[1] We describe an algorithm that retrieves the surface UVB (280–315 nm) and UVA (315–400 nm) irradiances from the Surface and Atmosphere Radiation Budget (SARB) product of Clouds and the Earth's Radiant Energy System (CERES). The SARB product we use here routinely calculates the vertical profiles of shortwave, longwave, and window channel irradiances with inputs of retrievals from imagers collocated with CERES. The top of the atmosphere broadband irradiance from SARB is constrained by CERES broadband irradiance. The shortwave spectrum in the SARB calculation is divided into 15 bands, and the two ultraviolet spectral bands, band 5 (298.5–322.5 nm) and band 6 (322.5–357.5 nm), are used to generate surface UVB and UVA irradiances. In this study, we develop a set of ratio lookup tables to derive surface UVB and UVA irradiances from SARB band 5 and band 6 outputs. We show that the ratio of band 5 to UVB irradiance is sensitive to total column ozone, solar zenith angle, surface albedo, and the atmospheric profile in cloud-free conditions; in cloudy conditions, the ratio of band 5 to UVB irradiance is also sensitive to cloud optical depth and height. Additionally, we show that the ratio of band 6 to UVA irradiance is sensitive to solar zenith angle, surface albedo, and cloud optical depth. We also derive a UV index from the UVB irradiance. Our algorithm may be applied at any surface elevation or surface type, including snow and ice. Surface UV irradiances derived from the lookup table that we created agree well with those computed by the high-resolution, multistream radiative transfer code, with differences ranging from –10% to +4% for UVB and UVA irradiances. The relative differences for the UV index are higher, ranging from –26% to +16%.

Citation: Su, W., T. P. Charlock, and F. G. Rose (2005), Deriving surface ultraviolet radiation from CERES surface and atmospheric radiation budget: Methodology, *J. Geophys. Res.*, 110, D14209, doi:10.1029/2005JD005794.

1. Introduction

[2] Since the 1980s substantial depletion of stratospheric ozone has been observed during later winter and spring, first over the Antarctic and then later over the Arctic. This is a result of increased atmospheric halogen loading induced by anthropogenic emissions [World Meteorological Organization, 2003]. The depletion of stratospheric ozone increases the ultraviolet (UV) radiation at the surface, with consequences for human health as well as plant growth on the Earth.

[3] UV radiation is divided into three bands: UVA (315–400 nm), UVB (280–315 nm), and UVC (100–280 nm). Ozone absorbs very little UVA radiation. UVA is associated with aging and reddening of the skin, as well as cataract

formation. Ozone strongly absorbs UVB, and UVB increased significantly at the surface in the early 1990s because of stratospheric ozone depletion [Kerr and McElroy, 1993; Herman *et al.*, 1996]. UVB is associated with squamous cell carcinoma, but not necessarily with basal cell carcinoma or melanoma. UVB is also associated with the beneficial production of vitamin D. Stratospheric ozone absorbs all UVC, so no UVC is observed on the ground. Slight exposure to the potent UVC can cause mutations and even death.

[4] An erythral (or sunburn) action spectrum has been introduced to represent the average skin response over the UVB and UVA spectral regions [McKinlay and Diffey, 1987]. This action spectrum is a composite of several investigators' measurements of the response of many different human skin types to UV radiation. Weighting the UVB and UVA irradiances by the action spectrum yields the erythral effective irradiance or "dose rate." This dose rate

represents the instantaneous amount of skin damaging UV radiation. Another term commonly used to indicate the UV intensity is UV index, which is expressed by multiplying the erythral effective irradiance by 40. The U.S. Environmental Protection Agency (EPA) has devised guidelines for use of the UV index.

[5] The potential threat of increased UV exposure to humans and plants has motivated a number of research and monitoring programs at national and international levels. Among the most significant achievements of the past decade has been the development of ground-based ozone and UV observation networks. Before the 1980s only a few stations conducted regular measurements, whereas now hundreds of ozone/UV stations are operating around the globe. Examples include the U.S. National Science Foundation (NSF) polar UV network [Booth *et al.*, 1995] and the U.S. Department of Agriculture (USDA) UV Monitoring network [Bigelow *et al.*, 1998], which are equipped with well-calibrated UV instruments and provide in situ ground measurements. However, the coverage of these surface networks is geographically limited; this limitation can be overcome with spaceborne remote sensing.

[6] UV radiation has been observed from space for 30 years and is used to derive both the total column ozone and the ozone profile [McPeters *et al.*, 1994]. Early UV radiation was measured by the Backscatter Ultraviolet (BUV) sensor on board the Nimbus 4 launched in 1970 [Heath *et al.*, 1975]. This was followed by the Total Ozone Mapping Spectrometer (TOMS) on Nimbus 7, which provided the longest spaceborne UV record (1978–1993) obtained from a single instrument. The TOMS instrument also flew on Meteor-3 from 1991 to 1994, and a TOMS now operates on the Earth-Probe satellite (since 1996). UV radiation has also been measured from Solar Backscatter Ultraviolet (SBUV), Stratospheric Aerosol and Gas Experiment (SAGE and SAGE II) and Global Ozone Monitoring Experiment (GOME) [Burrows *et al.*, 1999].

[7] These spaceborne sensors measure the radiances above the top of the atmosphere (TOA), and radiative transfer calculations are needed to derive the surface irradiances. Retrievals of surface UV irradiance from satellite data are based on simplifying assumptions, especially on the optical properties of aerosols, clouds, and surface albedo. For instance, the TOMS surface UV irradiance retrieval algorithm used tables generated from a plane-parallel radiative transfer model [Dave, 1964; Dave and Gazdag, 1970]. UV irradiances at the ground were tabulated for cloud-free and aerosol-free conditions via radiative transfer calculations that account for Rayleigh scattering, ozone absorption, terrain altitude and solar zenith angle (SZA) over a weakly reflecting surface (2–8%) [Eck *et al.*, 1995; Mayer *et al.*, 1998; Herman *et al.*, 1999]. They used climatological ozone profiles based on SBUV and surface reflectivity calculated from TOMS 380 nm backscattered radiances [Herman and Celarier, 1997]. Then the attenuation of UV by clouds was estimated with a correction factor, which was in turn determined by using TOMS 380 nm reflectivities or a plane-parallel cloud model with a homogeneous cloud located between 700 and 500 hPa [Eck *et al.*, 1995; Krotkov *et al.*, 2001]. Finally, the UV irradiance at the Earth's surface was calculated as the product of the clear-sky

irradiance and the cloud correction factor. Herman *et al.* [1997] used an aerosol index to account for aerosol absorption of the UV radiation in the TOMS algorithm. As the aerosol index tends to vanish for aerosols below about 1.5 km, absorption by boundary layer aerosols is not included. They applied the original TOMS UV algorithm over surfaces free of snow and ice [Eck *et al.*, 1995; Herman *et al.*, 1999], because the algorithm was unable to distinguish between snow or ice and clouds. The current TOMS UV algorithm [Kalliskota *et al.*, 2000], however, distinguishes between surface and cloud effects by introducing an empirical probability of the occurrence of cloud over snow. This reduces the error when averaged over periods of a month. Kalliskota *et al.* [2000] showed that TOMS retrievals overestimate surface UV dose for snow and ice free conditions by up to 25%, and underestimate the UV dose for snow/ice surface up to –35%, when compared with ground-based SUV-100 spectroradiometer measurements.

[8] Lubin *et al.* [1998] developed a global surface UV radiation climatology using broadband Earth Radiation Budget Experiment (ERBE) data, as well as the TOMS data. The ERBE monthly-hourly data were used to estimate the shortwave surface albedo and effective cloud optical depth. Then the retrieved surface albedo, effective cloud optical depth, and the monthly averaged total column ozone from TOMS were input to the spectrally resolved delta-Eddington algorithm of Joseph *et al.* [1976] to estimate the monthly average downwelling UV radiation at the surface for local noon. The resulting surface UV radiation climatology is useful for illustrating how surface UV radiation varies geographically in response to changes of ozone, cloud cover, and solar illumination. However, no tropospheric aerosol was included explicitly, as it was assumed that any significant aerosol optical depth over a grid box was approximated by the effective cloud optical depth.

[9] The lookup table (LUT) method was also used to generate a surface UV radiation data set over Europe using total column ozone from the GOME satellite [Verdebout, 2000]. Other parameters included in the LUT were SZA, surface elevation, surface UV albedo, cloud liquid water thickness retrieved from the Meteosat Visible and Infrared Imager, and near surface horizontal visibility to account for the aerosol effects. Clouds were assumed to have base height and thickness of 1 km, and droplet radii of 7 μm . The aerosol extinction coefficient at 550 nm was taken as 3 times the inverse of the visibility. The method did not account for variations in aerosol optical properties, as only one background standard aerosol model from Shettle [1989] was used. A UV surface albedo of 0.06 was assigned to ocean pixels and 0.03 to land pixels for regions free of snow and ice. For snow/ice pixels, the UV surface albedo was assumed to be 0.7.

[10] The algorithm and the database described here aim for an incremental advance on those mentioned above, mostly by exploiting new data on clouds produced by the Earth Observing System (EOS). The new algorithm generates surface UVB irradiance, UVA irradiance, and UV index by adjusting spectral irradiances contained in the Surface and Atmosphere Radiation Budget (SARB) component of the Clouds and the Earth's Radiant Energy

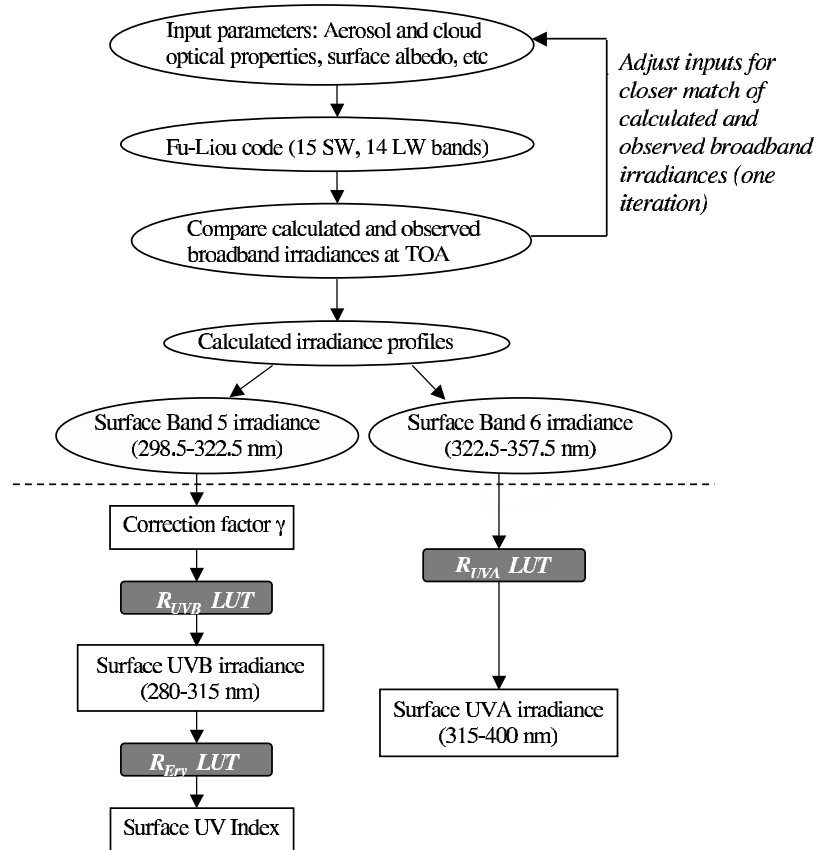


Figure 1. Process for determining surface UVB and UVA irradiance and UV index from CERES TOA measurements.

System (CERES), which is in turn based on fairly accurate retrievals of aerosol and cloud optical properties. The broadband shortwave (SW) SARB is the sum of calculations in 15 narrow bands, 2 of which we employ for our UV parameterization. CERES [Wielicki *et al.*, 1996] data are generated in two main formats: the instantaneous footprint (“CRS”) and the time-averaged grid box (“SYN”). As most users of UV irradiances would prefer gridded and time-averaged outputs, the algorithm described here documents the design of the UV component of SYN. SYN incorporates data from operational geostationary satellite, as well as from Tropical Rainfall Measuring Mission (TRMM), Terra, and Aqua. At this writing, none of the SYN products have been released.

[11] We create a set of lookup tables to derive surface spectral UV radiation from SARB surface irradiances, which are constrained by CERES TOA broadband measurements. Figure 1 is a flowchart depicting the process of generating surface UV radiation from the SARB output. In section 2, we briefly review the algorithm computes the SARB. The focus of this paper is the development of the LUTs for UV underneath the dashed line in Figure 1. We use a high-resolution radiative transfer model to develop the LUTs, and the model is validated with ground UV MFRSR measurements in section 3. The LUTs (gray boxes in Figure 1) adjust the outputs of SARB bands 5 and 6, which correspond roughly with UVB and UVA, to yield irradiances at the surface for the exact spectral intervals of UVB

and UVA. Section 4 covers more of the structure of the LUT. Section 5 compares the UVB and UVA that we parameterize from SARB parameters and the LUT, with the “true” UVB and UVA from the high-resolution model. A summary and a discussion are contained in section 6, and conclusions are in section 7.

2. CERES Surface and Atmosphere Radiation Budget Calculation

[12] The CERES instrument measures radiances in three channels: a broadband shortwave channel ($\sim 0.3\text{--}5\text{ }\mu\text{m}$), a window channel ($8\text{--}12\text{ }\mu\text{m}$), and a total channel ($\sim 0.3\text{--}100\text{ }\mu\text{m}$). The CERES radiances are converted to reflected shortwave (SW), emitted longwave (LW), and emitted window (WN) TOA irradiances. The large CERES footprints ($\sim 20\text{ km}$) of the TRMM satellite are matched with smaller Visible Infrared Scanner (VIRS) pixels, and the large CERES footprints of the Terra and Aqua satellites are matched with smaller Moderate Resolution Imaging Spectroradiometer (MODIS) pixels.

[13] The SARB product provides vertical profiles of SW, LW, and WN channels at the TOA, 70 hPa, 200 hPa, 500 hPa, and the surface for all-sky and clear-sky conditions [Charlock *et al.*, 2002] using the *Fu and Liou* [1993] two-stream radiative transfer code. Then the modeled TOA SW and LW irradiances are constrained to approach the CERES retrieved SW and LW irradiances by adjusting key input

parameters [Rose *et al.*, 1997; Charlock *et al.*, 1997; Rose and Charlock, 1999].

[14] Inputs for the SARB Fu-Liou calculation include aerosol and cloud optical properties, surface albedo, profiles of temperature, humidity, and ozone. Aerosol optical thickness (AOT) retrievals are based on VIRS [Ignatov and Stowe, 2000] when processing CERES TRMM data, and are based on MODIS [Kaufman *et al.*, 1997a] when processing CERES Terra and Aqua data. For grid boxes lacking a satellite-based retrieval, the AOT is from the NCAR Model for Atmospheric Transport and Chemistry (MATCH) assimilation [Collins *et al.*, 2001]. We always assign aerosol vertical profiles and aerosol types (i.e., fraction of sulfate, soot, etc.) from MATCH and use the spectral optical properties of Hess *et al.* [1998] and Tegen and Lacis [1996].

[15] Land surface albedos are specified according to the CERES surface property maps [Rutan and Charlock, 1997, 1999], which are keyed to International Geosphere-Biosphere Project (IGBP) land types. Ocean spectral albedo is obtained using a lookup table considering SZA, wind speed, chlorophyll concentration, and cloud/aerosol optical depth [Jin *et al.*, 2004]. We use daily global ozone profiles from Stratosphere Monitoring Ozone Blended Analysis (SMOBA) [Yang *et al.*, 1999]. We use temperature and humidity profiles from ECMWF [Rabier *et al.*, 1998] for TRMM and from the NASA Global Modeling and Assimilation Office (GMAO) for Terra and Aqua. Surface elevation is taken from the U.S. Geological Survey GTOPO30 digital elevation model.

[16] Cloud properties are the most critical inputs for the SARB calculation. We use retrievals of cloud optical depth, cloud phase (liquid or ice), effective droplet radius or ice crystal diameter, liquid water path or ice water path, and effective radiating temperature (with estimates of cloud top pressure and geometrical thickness) generated by the CERES team [Minnis *et al.*, 2002]. They are based on imager data (VIRS on TRMM, MODIS on Terra and Aqua, and ISCCP B1 geostationary radiances; see Rossow and Schiffer [1991] for ISCCP) and assume plane-parallel, and single-layered clouds [Minnis *et al.*, 2002]. All of the various imager pixels have higher spatial resolution than the coarse footprints of the broadband CERES instrument. The daytime retrieval technique [Arduini *et al.*, 2002] provides optical depth from a visible channel over snow-free areas, and the daytime snow retrieval technique [Platnick *et al.*, 2001] provides optical depth from a near infrared channel over snow-covered areas. A complex algorithm [Young *et al.*, 1998] combines and interpolates CERES measurements with geostationary results for hourly estimates of cloud properties and broadband TOA irradiances. Of the 24 hourly estimates of cloud properties in a grid box for one day, typically 8 will be from 3-hourly geostationary retrievals, 2 will be from MODIS or VIRS retrievals, and the remainder will be interpolated.

[17] The Fu-Liou code uses the properties mentioned above to calculate the irradiance profiles of SW, LW, and WN channels. The SW spectrum in the Fu-Liou code is divided into 15 bands, with band 4 (285.9–298.5 nm), band 5 (298.5–322.5 nm), and band 6 (322.5–357.5 nm) overlapping the UVB and UVA spectral range. In this study, we

focus on producing surface UVB and UVA irradiances using the outputs of band 5 and band 6 at the surface.

3. Validation of SBDART Radiative Transfer Model

[18] We use the multistream, high-resolution SBDART (Santa Barbara DISORT Atmospheric Radiative Transfer; see Ricchiazzi *et al.* [1998]) model to develop the LUTs to derive surface UVB irradiance from band 5 irradiance, and UVA irradiance from band 6 irradiance.

[19] We first tested the accuracy of SBDART in the UV spectrum by comparing with UV MFRSR (multifilter rotating shadowband radiometer) irradiance measurements. The data were provided by USDA for cloud-free conditions at the U.S. Department of Energy's Atmospheric Radiation Measurement (ARM) Southern Great Plains (SGP) site (36.6°N, 97.5°W) for 2001. The UV MFRSR measures total horizontal, direct normal, and diffuse horizontal irradiances at wavelengths of 300, 305, 311, 317, 326, 332, and 368 nm. It uses separate detectors for the bands, each having an ion-assisted deposition filter with a nominal 2 nm full width at half maximum bandwidth. Data are stored as 3-min averages.

[20] The Langley method is used to calibrate the ground-based UV MFRSR [Shaw, 1976]. The extraterrestrial solar irradiance thus derived from the UV MFRSR measurements was compared with the high-resolution Solar Ultraviolet Spectral Irradiance Monitor (SUSIM) ATLAS-3 solar irradiance [Bigelow and Slusser, 2000]. The SUSIM ATLAS-3 provides extraterrestrial solar irradiances from 110 to 410 nm with 0.15 nm resolution (http://www.solar.nrl.navy.mil/susim_atlas_data.html). The differences for all the seven channels were within 8%. We note that only two Langley events were observed for the 300 nm channel during the calibration period, so the 8% accuracy should be applied to the 300 nm channel with caution (which we discuss later).

[21] We focused the comparison of SBDART and UV MFRSR on 11 clear days during summer 2001. Each candidate 30-min interval of UV MFRSR data was screened for clouds with a minute-by-minute analysis of the collocated broadband radiometer record [Long and Ackerman, 2000]. We used the SUSIM ATLAS-3 extraterrestrial solar spectrum in SBDART simulations. Input data to SBDART included total column ozone, aerosol and cloud optical properties, surface elevation, atmospheric profiles (temperature, water vapor, ozone), and the surface spectral albedo. Total column ozone was provided by the USDA UV MFRSR [Gao *et al.*, 2001]. Spectral AOT was obtained from the SGP AERONET Cimel instrument [Holben *et al.*, 1998] at seven wavelengths from 340 nm to 1020 nm. Aerosol optical properties in the UV were obtained by fitting an internal mixture of water, sulfate, and black carbon to the aerosol size distribution and refractive index retrievals of Dubovik and King [2000], and then performing explicit Mie calculations of the optical depth, asymmetry factor, and single-scattering albedo at each wavelength [Schuster *et al.*, 2005]. Spectral albedo for the SGP site was obtained from helicopter measurements during a previous summer [Rutan *et al.*, 2003]. We used the climatological midlatitude summer atmospheric profile in SBDART. This selection of a climatological profile affects

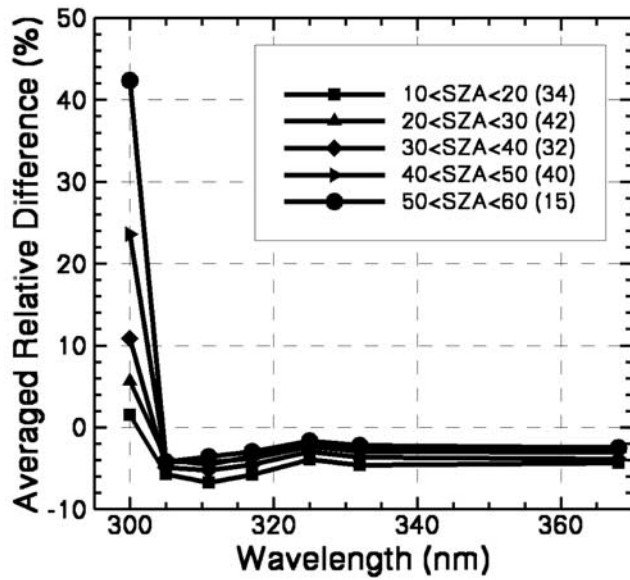


Figure 2. Averaged relative difference ϵ between measured (UV MFRSR) and simulated (SBDART) irradiances for five solar zenith angle bins. Numbers in parentheses are the total samples for each solar zenith angle bin.

the vertical distribution of ozone; and to a lesser extent, the ozone absorption coefficient, as it has some temperature dependence [Molina and Molina, 1986]. The water vapor profile has negligible impact on UV.

[22] SBDART was run with 8 streams at the resolution of 0.2 nm to simulate ground level spectral irradiances of the seven UV MFRSR channels for those cloud-free 30-min intervals having SZAs less than 60 degrees. The output of SBDART was convolved with the respective instrument spectral response function to generate filtered irradiances for each channel. Then the relative differences ϵ were calculated for the measured and simulated filtered irradiances:

$$\epsilon = \frac{F_{\text{meas}} - F_{\text{simu}}}{F_{\text{meas}}} \times 100\% \quad (1)$$

F_{meas} is the UV MFRSR measured irradiance and F_{simu} is the SBDART simulated irradiance. The relative differences were then binned according to SZA for all data available. The averaged relative differences for five SZA bins are shown in Figure 2. The relative differences in Figure 2 are less than 8% for all wavelengths except 300 nm, which is the UV MFRSR calibration precision [Bigelow and Slusser, 2000].

[23] The relative differences for the 300 nm channel, however, increases significantly with SZA; from less than 6% for SZAs less than 30° to 42% for SZAs between 50° and 60°. Possible causes of these larger discrepancies between measurement and simulation include (1) nonlinearity of the Langley plots at 300 nm [Schmid *et al.*, 1998] and (2) the diminution of the 300 nm signal with increasing SZA, resulting in signal-to-noise ratios which are too small for accurate measurements. Given this lack of confidence in calibration at 300 nm [i.e., Slusser *et al.*, 2000] and the agreement at the other UV MFRSR wavelengths, we

conclude that the accuracy of SBDART is acceptable for UV simulations.

4. Constructing Lookup Tables

[24] We now run SBDART with 8 streams for spectral irradiance from 280 to 400 nm at a resolution of 0.2 nm, and then integrate across appropriate wavelength regions to obtain irradiances in band 5, band 6, UVB, and UVA. We simulate irradiances for different aerosol types, AOT, cloud optical depth (COD), cloud effective height, total column ozone, SZAs, surface albedo, and atmospheric profiles. We examine the sensitivity of the ratios of band 5 to UVB irradiance, and band 6 to UVA irradiance, to these parameters. We then create a set of LUTs to enable CERES, which routinely computes two-stream Fu-Liou irradiances for bands 5 and 6 over the globe, to also generate accurate values for UVB and UVA irradiances at the surface. Furthermore, we parameterize the UV spectral irradiance weighted by the erythral action spectrum [McKinlay and Diffey, 1987] and calculate the UV index.

[25] The aerosol optical properties that we use in SBDART are from the Optical Properties of Aerosols and Clouds (OPAC) package [Hess *et al.*, 1998]. Table 1 summarizes the optical properties (at wavelength of 550 nm and relative humidity of 50%) for the aerosol types that we used in our simulation. The aerosol type names in parentheses indicate the short names that we use in figure legends. We include eight types of OPAC aerosols in Table 1, pairing each with a specific AOT at 550 nm. Table 1 encompasses a wide range of spectral AOTs, single-scattering albedos and asymmetry factors.

4.1. Inferring UVB From Band 5 Irradiances

[26] UVB and band 5 overlap from 298.5 nm to 315 nm. Clouds, aerosols, surface albedo, SZA, and total column ozone can significantly affect irradiances in the overlap interval. To derive surface UVB irradiance from band 5 irradiance, we define the ratio of band 5 irradiance to UVB irradiance:

$$R_{\text{UVB}} = \frac{F_{\text{SBDART}}^5}{F_{\text{SBDART}}^{\text{UVB}}} \quad (2)$$

where F_{SBDART}^5 is the band 5 irradiance calculated with SBDART, and $F_{\text{SBDART}}^{\text{UVB}}$ is the UVB irradiance calculated

Table 1. OPAC Aerosol Model Parameters at 550 nm^a

	Aerosol Optical Thickness	Single-Scattering Albedo	Asymmetry Factor
Arctic	0.05	0.84	0.69
Continental average (ContiAvg)	0.11	0.89	0.67
Continental clean (ContiCln)	0.05	0.96	0.68
Continental polluted (ContiPol)	0.24	0.85	0.67
Desert	0.27	0.88	0.73
Maritime clean (MaritCln)	0.07	0.97	0.76
Maritime polluted (MaritPol)	0.09	0.96	0.74
Maritime tropical (MaritTrp)	0.04	1.00	0.76
Urban	0.26	0.76	0.65

^aSee Hess *et al.* [1998]. Abbreviated names for each aerosol type are given in parentheses with corresponding default spectral AOT in next column. Single-scattering albedo and asymmetry factor are specified for relative humidity of 50%.

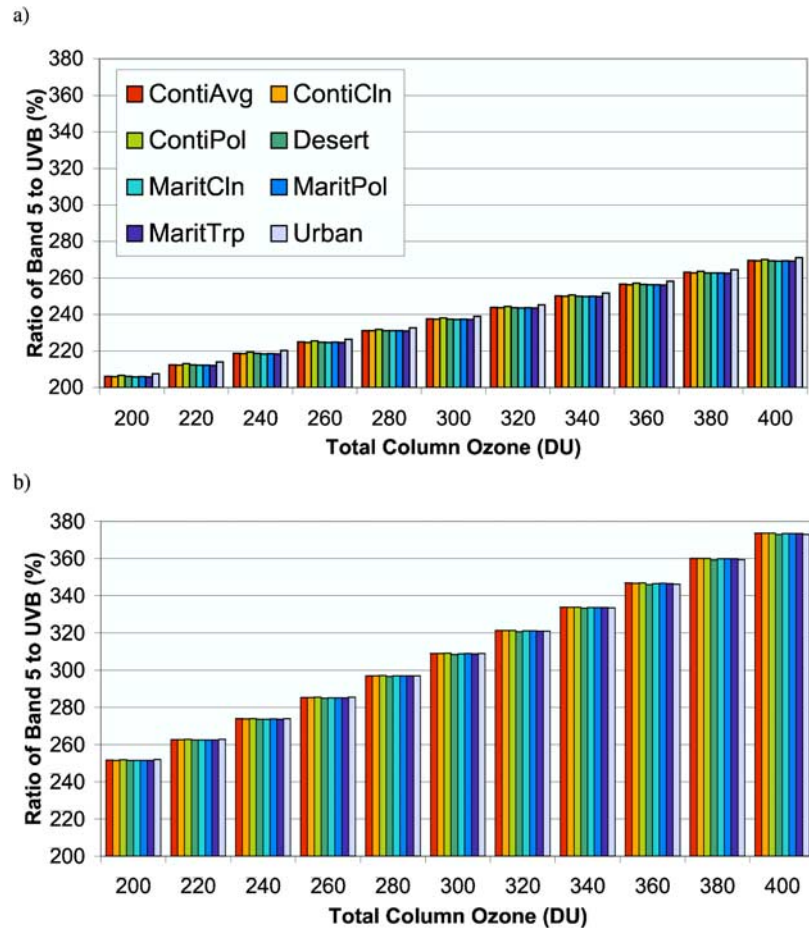


Figure 3. Sensitivity of ratios R_{UVB} of band 5 to UVB irradiance to aerosol condition (color bar) at 11 discrete ozone loadings (200 to 400 DU in steps of 20 DU) for midlatitude summer atmosphere, ocean surface albedo in clear sky. (a) SZA = 30° and (b) SZA = 60°.

with SBDART. We can calculate the surface UVB irradiance from the ratio of R_{UVB} , if the band 5 irradiance is known. In the following we build LUTs of R_{UVB} separately for cloud-free and cloudy conditions.

4.1.1. UVB Irradiance Ratio for Cloud-Free Conditions

[27] For cloud-free conditions, we calculated the ratio R_{UVB} for 4774 cases: (1) SZA: 0° to 60° in steps of 10°; (2) total column ozone: 200 DU to 400 DU in steps of 20 DU; (3) atmospheric profiles: tropical, midlatitude summer, midlatitude winter, subarctic summer, and subarctic winter; (4) for each atmospheric model, several relevant surface albedos (including grassland, desert, ocean, snow, and ice) are used; (5) different OPAC aerosols types as in Table 1.

[28] Figure 3 shows the sensitivity of ratio R_{UVB} to the eight aerosol conditions of Table 1 at various ozone loadings (DU). This simulation is done for a clear midlatitude summer atmosphere over ocean, at SZAs of 30° and 60°. The abbreviated aerosol type names in the parentheses of Table 1 are used in the legends of Figure 3 and other figures. Note the sensitivity of R_{UVB} (Figure 3) to total column ozone and SZA. While the AOTs at 550 nm of continental clean and urban aerosols in Table 1 differ by an order of magnitude, the R_{UVB} among the various aerosol conditions

differ less than 2%, at any fixed set of both total column ozone and SZA (Figure 3). Since this parameterization will be implemented by CERES with satellite-based retrievals of AOT for which errors generally exceed the 2% sensitivity of AOT on R_{UVB} [Mishchenko *et al.*, 1999; Tanre *et al.*, 1999; Kaufman *et al.*, 1997b; Coakley *et al.*, 2002], we further ignore the effect of aerosols on the ratio R_{UVB} . UVB is sensitive to aerosols, but R_{UVB} is not.

[29] Figure 4 shows the effect of surface albedo on ratio R_{UVB} , for a subarctic winter atmosphere with Arctic aerosols at a SZA of 60°. Here we consider three types of surface albedos: ice, sea, and snow. R_{UVB} for sea surface and ice/snow surface differ by roughly 1% for total column ozone of 300 DU and about 2.5% for total column ozone of 400 DU, indicating that the effect of surface albedo becomes more prominent at higher ozone loadings. As it is not unusual to have total column ozone up to 400 DU at high latitude during the spring melt, we investigate a wide range of values for surface albedo. Tests with ocean, grassland, and desert surface albedo values, show a range of only 0.5% for the ratio R_{UVB} . So only two types of surfaces are considered here: high albedo (ice and snow) and low to moderate albedo (all others).

[30] Figure 5 shows the influences of five different atmospheric profiles on the ratios R_{UVB} for a SZA of 30°

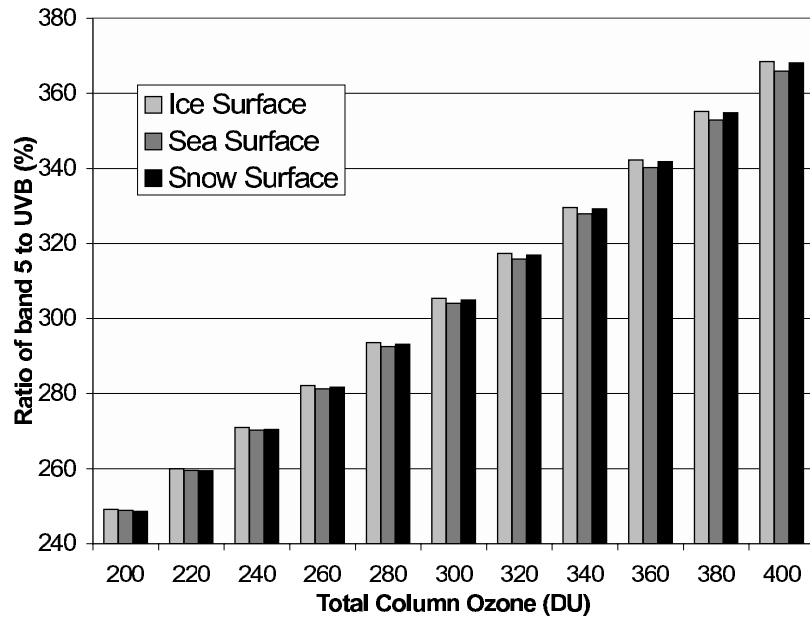


Figure 4. Effect of surface albedo (shaded bars) on ratios R_{UVB} of band 5 to UVB irradiance at 11 discrete ozone loadings (200 to 400 DU in steps of 20 DU) for the subarctic winter atmosphere, Arctic aerosols, and SZA of 60° .

and continental clean aerosols. The atmospheric profiles, which apportion ozone with pressure and temperature, induce a range of 5% in R_{UVB} for a given total column ozone. This is mostly due to the temperature dependence of the ozone cross section, as indicated by *Molina and Molina* [1986]. Hence we include the different atmospheric profiles in the LUT for the R_{UVB} .

[31] We note above that R_{UVB} is sensitive to SZA, total column ozone, surface albedo and atmospheric profile;

but not to aerosols. For clear skies, we fit the R_{UVB} as a second-order polynomial of total column ozone. We tabularize the regression coefficients for R_{UVB} separately for high- and low-albedo surfaces, for each combination of the 7 SZAs and the 5 atmospheric profiles.

4.1.2. UVB Irradiance Ratio for Cloudy Conditions

[32] Clouds can reduce the surface UV radiation significantly. Hence, in addition to the variables that we tested for clear conditions, we now examine cloud optical depth

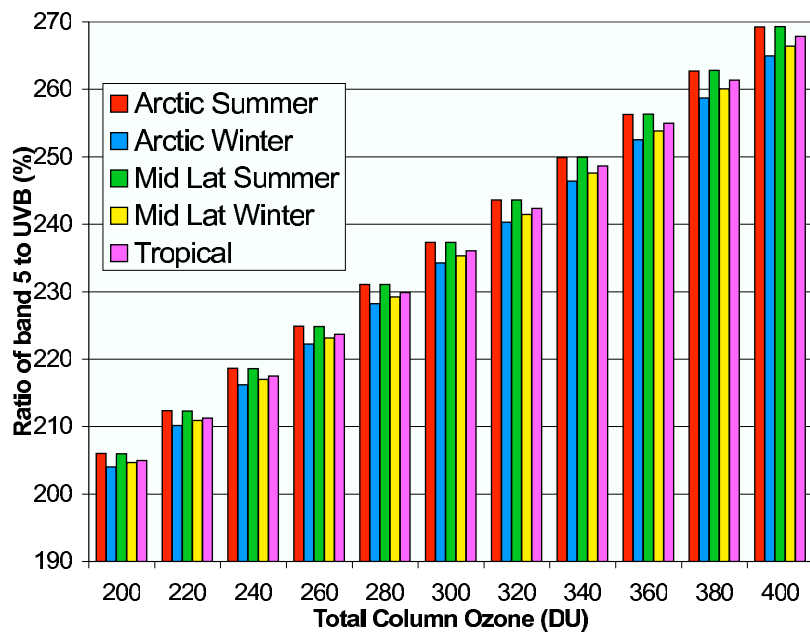


Figure 5. Effect of atmospheric profiles (color bar) on ratios R_{UVB} of band 5 to UVB irradiance at 11 discrete ozone loadings (200 to 400 DU in steps of 20 DU) for SZA of 30° , sea surface, and continental clean aerosols.

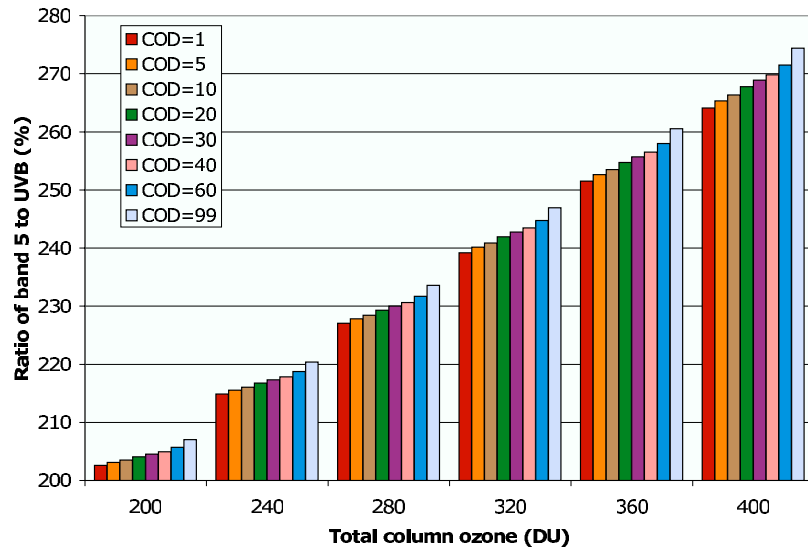


Figure 6. Impact of cloud optical depth (COD) on ratios R_{UVB} of band 5 to UVB irradiance for 6 discrete ozone loadings (200 to 400 DU in steps of 40 DU), midlatitude summer atmosphere, OPAC continental average aerosols, grassland surface, and SZA = 30°. Ratios R_{UVB} are given for 8 values of COD (color bars), all having cloud bottom (top) at 1 km (3 km).

(COD) and cloud effective height (H). Since the effect of clouds on surface UV radiation is usually much larger than the effect of aerosols (recall that the aerosol effect on R_{UVB} is less than 2% in cloud-free conditions), only one aerosol type (continental average) is considered for cloudy cases. Ratios R_{UVB} of band 5 irradiance to UVB irradiance were calculated for the following 17,520 cases: (1) SZA: 0° to 60° in steps of 10°; (2) total column ozone: 200 DU to 400 DU in steps of 40 DU; (3) cloud optical depth: 1, 5, 10, 20, 30, 40, 60, 99; (4) cloud effective height: 2.0 (bottom at 1 km and top at 3 km, 1–3 km), 4.5 (3–6 km), 9.0 km (8–10 km); (5) atmospheric models: tropical, midlatitude summer, midlatitude winter, subarctic summer, and subarctic winter; (6) for each atmospheric model, several relevant surface albedos are used.

[33] Figure 6 shows the ratio R_{UVB} at various CODs for 6 discrete values of total column ozone (200, 240, 280, 320, 360, and 400 DU). The cloud effective height is 2 km. The simulation is done for the midlatitude summer atmosphere, continental average aerosols, grassland surface, 30° SZA. We use cloud droplet radius of 10 μm in all of these cloudy cases (changes in cloud droplet radius are not significant for R_{UVB}). The ratios increase by about 5% for COD changes from 1 to 99 at a total column ozone of 200 DU, and increase by about 15% for total column ozone of 400 DU.

[34] Cloud effective height (H) significantly influences the exposure of tropospheric ozone to multiple scattering; the impact of H on the R_{UVB} ratios is shown in Figure 7. This simulation is done for the subarctic summer atmosphere over an ice surface, a SZA of 30°, and a COD of 30. Figure 7 indicates that the R_{UVB} ratio for H of 9 km is 25% higher than the R_{UVB} ratio for H of 2 km when, total column ozone is 400 DU. We also test the sensitivity of R_{UVB} on surface albedo and atmospheric profile as in the cloud-free cases.

[35] Similar to the clear-sky R_{UVB} , the cloudy sky R_{UVB} is also sensitive to SZA, total column ozone, surface albedo

and atmospheric profile; but not to aerosols. Figures 6 and 7 show the need for two additional dimensions, COD and H, in the LUT for cloudy sky R_{UVB} . We fit the corresponding cloudy sky R_{UVB} ratio as a second-order polynomial of total column ozone. The regression coefficients for cloudy sky R_{UVB} are tabulated separately for high- and low-albedo surfaces, for each combination of the 7 SZAs, the 8 CODs, the 3 Hs, and the 5 atmospheric profiles.

4.2. Inferring UVA From Band 6 Irradiances

[36] UVA and the band 6 overlap from 322.5 to 357.5 nm. SBDART is again used to simulate the UVA and band 6 irradiances. Similar to the ratio method used for band 5 and UVB, we define the ratio of band 6 irradiance to UVA irradiance:

$$R_{UVA} = \frac{F_{SBDART}^6}{F_{SBDART}^{UVA}} \quad (3)$$

where F_{SBDART}^6 is the band 6 irradiance calculated with SBDART, and F_{SBDART}^{UVA} is the UVA irradiance calculated with SBDART.

4.2.1. UVA Irradiance Ratio for Cloud-Free Conditions

[37] We calculate UVA and band 6 irradiances for the same 4774 cloud-free cases for which we calculate UVB and band 5 irradiances. The sensitivity of R_{UVA} to aerosol condition and total column ozone is shown in Figure 8, for a midlatitude summer atmosphere, ocean surface albedo, and 30° SZA. For the eight OPAC aerosol types tested at fixed values of total column ozone, R_{UVA} changes less than 1.5%. While for total column ozone ranging from 200 DU to 400 DU at fixed aerosol condition, R_{UVA} changes less than 0.3%. For low-albedo surfaces, such as ocean, grassland, and desert, the influences of changes in surface albedo on the ratio R_{UVA} are quite small, less than 0.1% (not shown). However, R_{UVA} values are about 2% larger for high-albedo surfaces, such as snow and ice, when compared with R_{UVA} for low-albedo surfaces (not shown). Different atmospheric

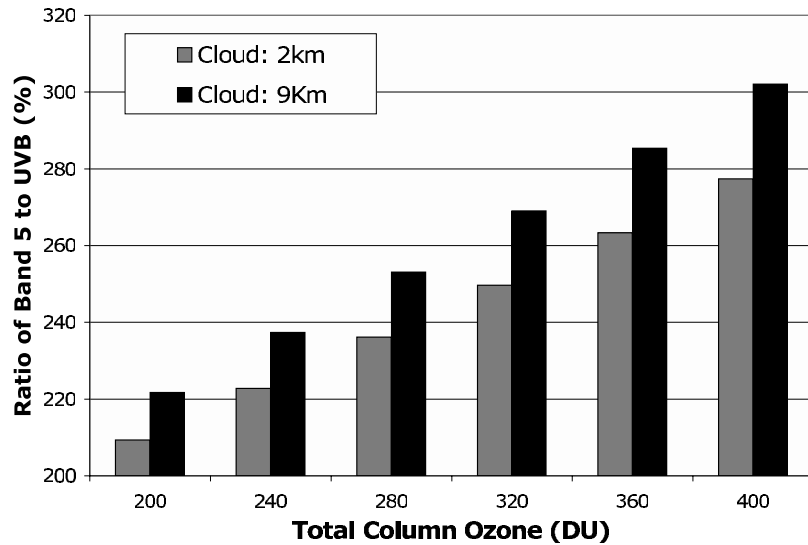


Figure 7. Impact of cloud effective height (H) on ratios R_{UVB} of band 5 to UVB irradiance for 6 discrete ozone loadings (200, 240, 280, 320, 360, and 400 DU). H of 2 km in gray has bottom (top) at 1 km (3 km). H of 9 km in black has bottom (top) at 8 km (10 km). All are for subarctic summer atmosphere, ice surface, cloud optical depth (COD) of 30, and SZA of 30° .

profiles virtually have no effects (0.1%) on the ratio R_{UVA} (not shown).

[38] For cloud-free conditions, the ratio R_{UVA} of band 6 to UVA is sensitive to surface albedo, SZA, and aerosols, but not sensitive to atmospheric profiles and total column ozone content. The errors in satellite-based retrievals of AOT (mentioned earlier) are much larger than the $\sim 1.5\%$ range in R_{UVA} due to changes in aerosol properties. Thus we ignore the effects of changes in aerosols and ozone on R_{UVA} . The LUTs for the ratio R_{UVA} are tabulated separately for high- and low-reflection surfaces for each given SZA.

4.2.2. UVA Irradiance Ratio for Cloudy Conditions

[39] For cloudy conditions, the ratios R_{UVA} of band 6 irradiance to UVA irradiance were simulated for the same 17520 cases mentioned in the earlier section on cloudy conditions for band 5 and UVB. Similar to R_{UVB} , the R_{UVA} ratios are not sensitive to changes in cloud droplet radius. In addition to all the variables that we tested for the cloud-free conditions, we also consider the effects of COD and cloud effective height on the ratio R_{UVA} .

[40] The effect of COD on the R_{UVA} ratio is shown in Figure 9. We calculate the R_{UVA} ratios for the midlatitude

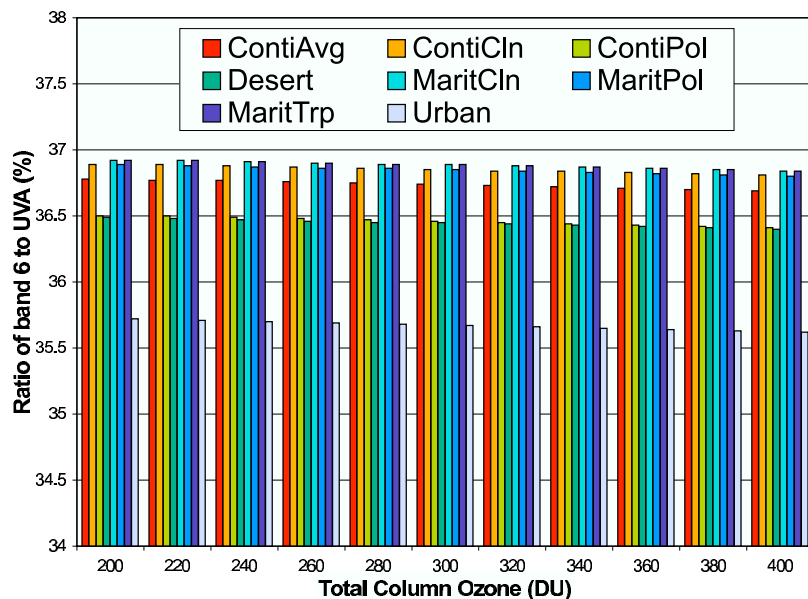


Figure 8. Impact of aerosol conditions (color bar) in clear skies on ratio R_{UVA} of band 6 to UVA irradiance for 11 discrete ozone loadings (200 to 400 DU in steps of 20 DU). All are for midlatitude summer atmosphere, sea surface albedo, and SZA of 30° . Aerosol conditions are given in Table 1.

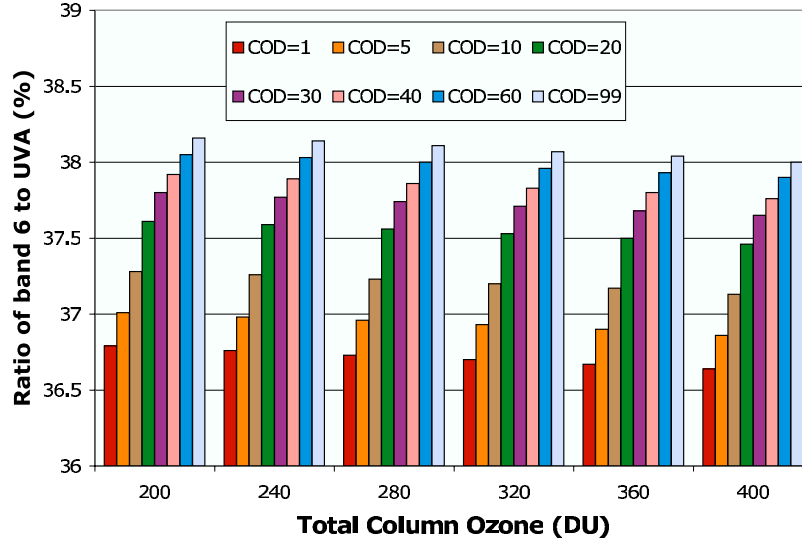


Figure 9. Impact of cloud optical depth (COD, in color) on ratios R_{UVA} of band 6 to UVA irradiance for 6 discrete ozone loadings (200 to 400 DU in steps of 40 DU). All are for midlatitude summer atmosphere, OPAC continental average aerosols, grassland surface, and SZA of 30° . Clouds have bottom (top) at 1 km (3 km).

summer atmosphere, grassland surface, continental average aerosols, 30° SZA, for eight different CODs. In this case the cloud effective heights are 2 km. As COD ranges from 1 to 99, the R_{UVA} ratio changes by about 1.5%. Cloud effective height has very small effect on the R_{UVA} , about 0.2% between H of 9 and 2 km (figure not shown).

[41] For cloudy conditions, the R_{UVA} ratio is sensitive to SZA, surface albedo, and COD. We include SZA, surface albedo, and COD in the LUT of the ratio R_{UVA} .

4.3. Erythral Irradiance

[42] Biological and medical researchers employ an erythral irradiance F_{Ery} . This is defined as the UVB and UVA weighted with the erythral (sunburn) action spectrum. An action spectrum expresses the impact of radiation on a biological system at each wavelength, as a fraction of the impact at a standard wavelength.

[43] The erythral action spectrum drops rapidly for wavelengths longer than 315 nm. UVB contributes enormously to the erythral irradiances. We define the ratio R_{Ery} of erythral irradiance to UVB irradiance as

$$R_{Ery} = \frac{F_{Ery}}{F_{SBDART}^{UVB}} = \frac{\int_{200}^{400} F_{SBDART}(\lambda) E(\lambda) d\lambda}{F_{SBDART}^{UVB}} \quad (4)$$

where $E(\lambda)$ is the erythral action spectrum. The UV index is simply the erythral irradiance (F_{Ery}) multiplied by 40.

4.3.1. Erythral Irradiance Ratio in Cloud-Free Conditions

[44] As with UVB and UVA, the effects of aerosols, surface albedo, atmospheric profiles, and total column ozone on R_{Ery} were tested using the 4774 cases specified earlier. Figure 10 shows the sensitivity of ratios R_{Ery} to changes in aerosol conditions at discrete values of total column ozone; here for a midlatitude summer atmosphere, ocean surface albedo, and SZA of 30° . The aerosols in Figure 10 vary widely in both amount and optical type

(Table 1), but aerosol affects R_{Ery} by only 0.2%. The ratio R_{Ery} does change with total column ozone content, dropping about 3% from 200 DU to 400 DU. The ratios R_{Ery} are sensitive to SZA but not to surface albedo; R_{Ery} differs by less than 0.3% when computed alternately with high-albedo (ice) and low-albedo (ocean) surfaces, using a subarctic winter atmosphere and clean continental aerosols. We also compared the ratio R_{Ery} for five atmospheric profiles, all using identical total column ozone; changes in the atmospheric profiles caused the R_{Ery} to vary less than 0.2%.

[45] For cloud-free conditions, the ratio R_{Ery} is a third-order polynomial as a function of total column ozone. We construct the LUT of the regression coefficients for different SZAs.

4.3.2. Erythral Irradiance Ratio in Cloudy Conditions

[46] For cloudy conditions, the ratio R_{Ery} was calculated for the 17,520 cases used earlier for UVB and UVA. Our tests indicate that R_{Ery} is not sensitive to cloud droplet radius, so we use $10 \mu\text{m}$ in all cloudy cases. Figure 11 shows the ratios R_{Ery} for different COD with a midlatitude summer atmosphere, grassland surface, OPAC continental average aerosols, and SZA of 30° . For COD ranging from 1 to 99, the ratio R_{Ery} varies by 0.2% (at total column ozone of 400 DU) to 0.6% (at 200 DU). Cloud effective height has even smaller impact on R_{Ery} (not shown).

[47] For cloudy conditions, the ratio R_{Ery} is a third-order polynomial as a function of total column ozone (DU). We tabularize the regression coefficients for combinations of SZA and COD.

5. Validation of the Retrieval Against Modeling Results

[48] In section 4 we developed a set of LUTs to derive surface UVB and UVA irradiances from band 5 and band 6 irradiances, and UV index from UVB irradiance. Since the

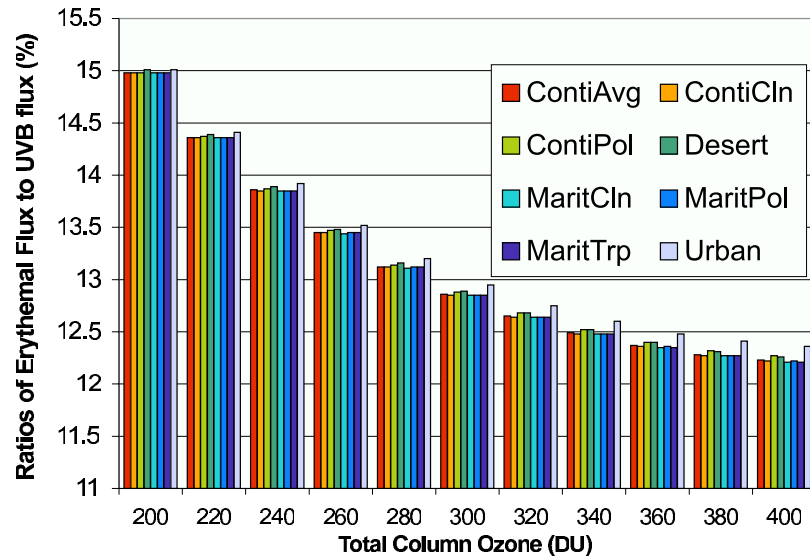


Figure 10. Impact of aerosol conditions (color bar) in clear skies on ratio R_{Ery} of erythemal irradiance to UVB irradiance for 11 discrete ozone loadings (200 to 400 DU in steps of 20 DU). All are for midlatitude summer atmosphere, sea surface albedo, and SZA of 30° . Aerosol conditions are given in Table 1.

ratio LUTs were calculated using the SBDART code, but we plan to apply them to the SARB Fu-Liou band 5 and 6 outputs, we must first check the consistency between the eight-stream SBDART band 5 and band 6 irradiances and the two-stream Fu-Liou band 5 and band 6 irradiances.

5.1. Comparison of SBDART Simulation With Fu-Liou Simulation

[49] Table 2 lists the irradiances for band 5 and band 6 calculated from the two-stream Fu-Liou and the 8-stream SBDART for SZA of 0° , 30° , 60° , and a climatological continental aerosol model [d'Almeida *et al.*, 1991] with

AOT = 0.5 at 500 nm. For band 5, the differences between SBDART and Fu-Liou are less than 6% for overhead sun; less than 10% for SZA = 30° ; and range between 12% and 30% for SZA = 60° . For band 6, the differences between SBDART and Fu-Liou are less than 2% (and within our target accuracy as a UV product for biological applications). The differences of SBDART and Fu-Liou seen in Table 2 are reduced for smaller AOT (not shown). The significant differences between band 5 irradiances calculated from Fu-Liou code and SBDART are due to different treatments of ozone absorption. Fu-Liou uses only a single correlated k for ozone in band 5, and the ozone cross section changes by

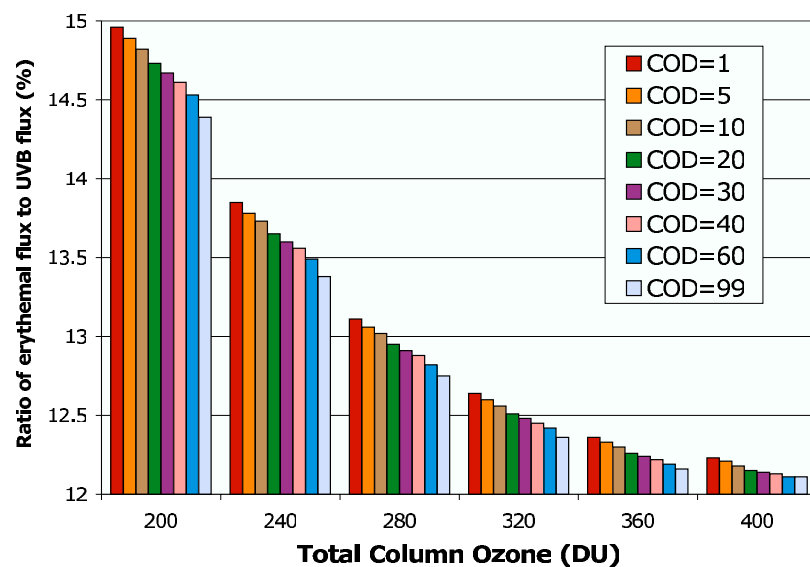


Figure 11. Impact of cloud optical depth (COD, in color) on ratios R_{Ery} of erythemal irradiance to UVB irradiance for 6 discrete ozone loadings (200 to 400 DU in steps of 40 DU). All are for midlatitude summer atmosphere, OPAC continental average aerosols, grassland surface, and SZA of 30° . Clouds have bottom (top) at 1 km (3 km).

Table 2. Irradiances From SBDART and Fu-Liou for Band 5 (298.5–322.5 nm) and Band 6 (322.5–357.5 nm) for Solar Zenith Angles of 0°, 30°, and 60°^a

Ozone, DU	SZA, deg	Fu-Liou Band 5	SBDART Band 5	Fu-Liou Band 6	SBDART Band 6
240	0	4.92	4.88	23.01	22.56
240	30	3.64	3.67	18.72	18.35
240	60	1.04	1.18	8.35	8.06
280	0	4.47	4.53	22.92	22.49
280	30	3.26	3.39	18.64	18.28
280	60	0.86	1.06	8.29	8.01
320	0	4.07	4.23	22.83	22.43
320	30	2.92	3.15	18.56	18.22
320	60	0.72	0.96	8.23	7.97
360	0	3.70	3.96	22.75	22.36
360	30	2.62	2.93	18.48	18.16
360	60	0.60	0.88	8.17	7.92

^aIrradiances are given in W/m². Aerosol type is the *d'Almeida et al.* [1991] continental aerosol, and aerosol optical depth is 0.5.

about an order of magnitude in this spectral region. In contrast, the computationally intensive SBDART utilizes parameterizations of high-resolution (5 cm⁻¹) ozone cross-section data [Molina and Molina, 1986]. The Fu-Liou errors in bands 5 and 6 (considered here as differences with SBDART) are not significant for the broadband radiation budget (for which the fast Fu-Liou code was explicitly designed). However, in order to provide sufficiently accurate UVB dosages with our lookup tables generated from SBDART simulations, the larger relative differences in band 5 require some correction.

[50] We define a band 5 correction factor γ as

$$\gamma = \frac{F_{Fu-Liou}^5}{F_{SBDART}^5} \quad (5)$$

where $F_{Fu-Liou}^5$ is the Fu-Liou band 5 irradiance, and F_{SBDART}^5 is the SBDART band 5 irradiance. We calculate the correction factor γ for SZA from 0° to 60° in intervals of 10° and conditions with various total column ozone, surface albedo, aerosol type from *d'Almeida et al.* [1991], and AOT. The correction factor γ varied by less than 0.01 (1%) for the variety of standard aerosol types and AOTs considered here (provided the other conditions were held fixed); so γ is effectively insensitive to changes in aerosol type or AOT. Figure 12 shows, however, that γ drops significantly with increasing total column ozone content, and that γ varies with SZA (i.e., a longer ozone path length requires more adjustment to Fu-Liou band 5). Varying surface albedo between 0 and 0.8 changes γ by about 3.5% for SZA = 0° and 2.5% for SZA = 60°. Fortunately, surface albedos less than 0.4 yield a range for γ of less than 1%. Hence we developed correction factors separately for two surface types: those with UV spectral albedo less than and greater than 0.4. The correction factors of the two albedo categories are each expressed by functions consisting of a second-order polynomial of total column ozone (DU) for each SZA.

[51] The target surface UVB irradiance (here considered as F_{SBDART}^{UVB} from SBDART) can be derived from operational Fu-Liou band 5 output using equation (2) (where R_{UVB} is essentially a spectral conversion of band 5 to UVB) and equation (5) (where γ corrects the economical Fu-Liou band 5 calculation) as

$$UVB = F_{SBDART}^{UVB} = \frac{F_{SBDART}^5}{R_{UVB}} = \frac{F_{Fu-Liou}^5}{R_{UVB} \times \gamma(\alpha, SZA)} \quad (6)$$

This combination of R_{UVB} and γ results in a fourth-order polynomial. For cloud-free conditions, the regression coefficients are derived for all combinations of the 7 values of SZAs, the 2 values of surface albedos, and the 5 atmospheric profiles. These combinations are used for cloudy conditions, but then CODs (8 values) and cloud effective heights (3 values) are also added to build the regression coefficients.

[52] No correction is needed for band 6 because of the good agreement between band 6 calculated from SBDART and Fu-Liou code. We need only the spectral conversion (R_{UVA}) of band 6 to UVA in equation (3). The surface UVA irradiance (here considered as F_{SBDART}^{UVA} from SBDART) can be derived from operational Fu-Liou band 6 according to equation (3):

$$UVA = F_{SBDART}^{UVA} = \frac{F_{SBDART}^6}{R_{UVA}} = \frac{F_{Fu-Liou}^6}{R_{UVA}} \quad (7)$$

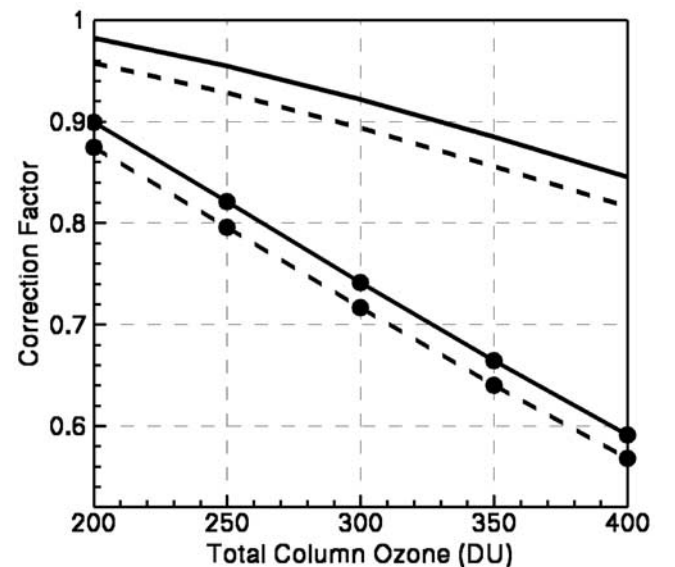


Figure 12. Averaged band 5 correction factors γ of different aerosol cases for low-albedo (solid lines) and high-albedo surfaces (dashed lines) for SZA = 20° and SZA = 60° (lines with circles).

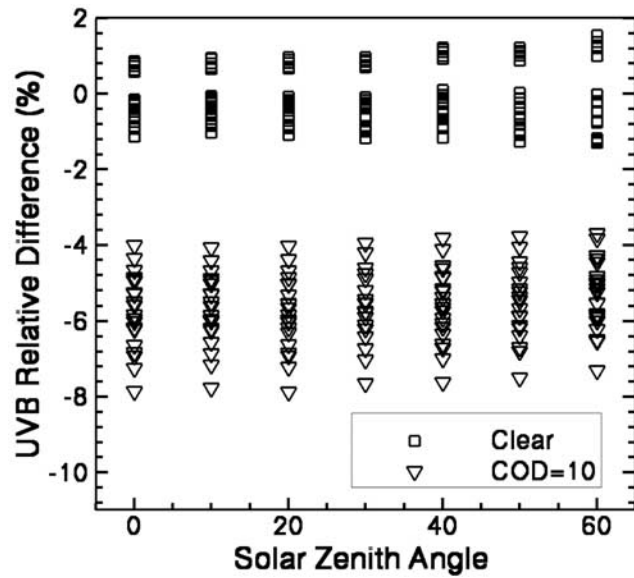


Figure 13. Relative differences between UVB “retrieved” from SARB and “true” UVB output from SBDART simulation for different solar zenith angles.

5.2. Comparison of Idealized Retrieval With Modeling Results

[53] With the LUTs that we developed in section 4 and the correction factor described in section 5.1, we compare the UVB, UVA, and UV index derived from SARB band 5 and band 6 irradiances generated by Fu-Liou code via the LUTs, with the “true” values simulated by SBDART. First, we run the Fu-Liou code for a midlatitude summer atmosphere with continental aerosols from *d’Almeida et al.* [1991], which differ from the OPAC aerosols used to develop the regression coefficients for the LUTs, for the following cases: (1) SZA: 0° to 60° , in steps of 10° ; (2) total

column ozone: 200 to 400 DU, in steps of 50 DU; (3) surface albedo: 0.0, 0.2, 0.4, 0.8; (4) aerosol optical thickness (AOT): 0.1, 0.2, 0.4, 0.8; (5) cloud optical depth (COD): 0, 1, 10, 100; (6) cloud height: base 7 km and top 8 km.

[54] Then the R_{UVB} LUTs and the correction factor γ are applied to band 5 irradiances calculated from Fu-Liou code to produce the “retrieved” UVB irradiance (equation (6)), and the R_{UVA} LUTs are applied to band 6 irradiances calculated from Fu-Liou code to produce the “retrieved” UVA irradiance (equation (7)). In addition, the R_{Ery} LUTs are applied to “retrieved” UVB irradiances to produce the “retrieved” UV index. SBDART is used to simulate the “true” UVB and UVA irradiances, and the UV index for the same cases. We calculate the relative differences (true minus retrieved, then divided by true value, and finally multiplied by 100% as in equation (1)) for each SZA, surface albedo, AOT and COD. Figure 13 shows the relative difference of UVB irradiance versus SZA for clear and COD = 10, with AOT = 0.1 and for all surface albedos. For cloud-free conditions, the relative differences for UVB are between -2% and 2% ; relative differences for UVB become more negative with clouds, and range from -8% to -4% for COD = 10. Figure 14 is the same as Figure 13, but for the UVA irradiance. For cloud-free cases, the relative differences for UVA range from -4% to 1% ; and for COD = 10, the relative differences are from -6% to 0% . The relative differences for the UV index (Figure 15) are much larger than the cases of UVB (Figure 13) and UVA (Figure 14), because it uses successive LUTs (for UVB and erythral irradiance). For cloud-free cases, the relative differences for the UV index are small, within $\pm 4\%$; but for cloudy cases, the relative differences are large and range from -20% to 16% for COD = 10. Larger relative differences are tolerated for the cloudy cases, because the surface UV dosage tends to be much smaller under cloudy skies (and the UV index is typically rounded to the closest integer). These comparisons indicate that the LUTs are

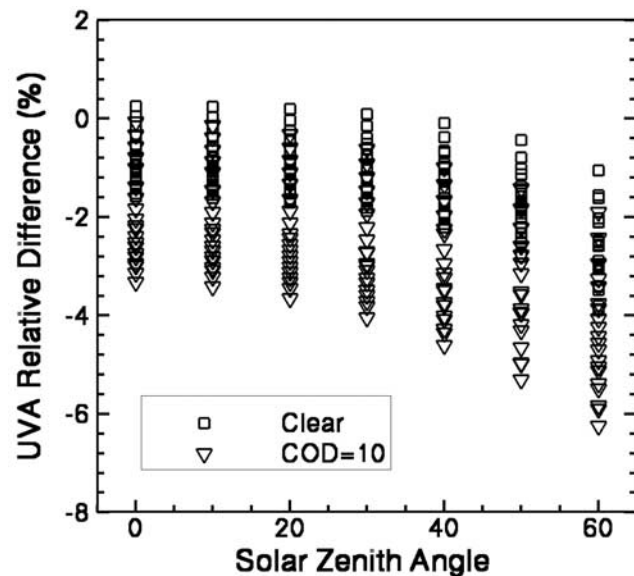


Figure 14. Same as Figure 13, but for UVA.

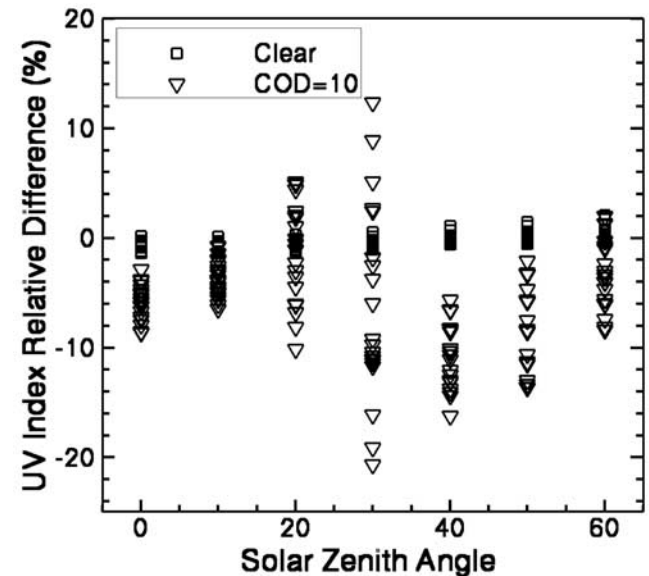


Figure 15. Same as Figure 13, but for UV index.

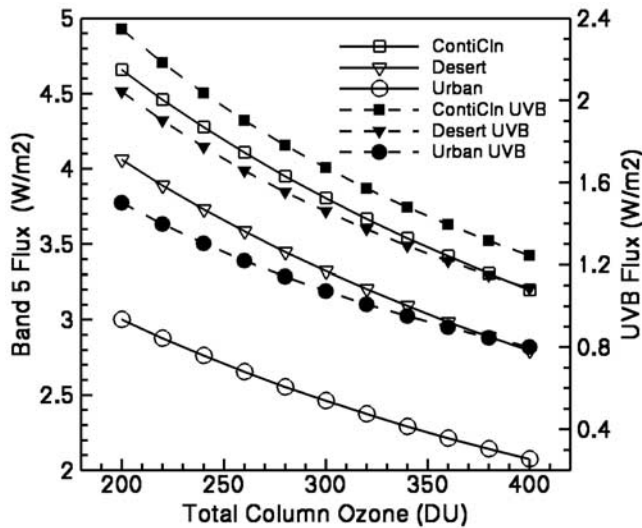


Figure 16a. Total surface downwelling band 5 (solid lines) and UVB (dashed lines) irradiances for different OPAC aerosols for midlatitude summer atmosphere, grassland surface, and solar zenith angle of 30° .

acceptable for use in satellite retrievals of the surface UVB irradiance, UVA irradiance, and UV index.

6. Summary and Discussion

[55] We have described a parameterization to convert band 5 (298.5–322.5 nm) irradiance to UVB (280–315 nm) irradiance, and band 6 (322.5–357.5 nm) irradiances to UVA (315–400 nm) irradiance. The conversions are done via a set of lookup tables that we developed with calculations from the multistream high-resolution radiative transfer model SBDART. This allows us to obtain surface UV irradiance from the intricate SARB computation constrained by CERES broadband irradiances. SARB incor-

porates data from EOS and other operational platforms (including geostationary) and an aerosol assimilation, thereby accounting for the effects of temporal and geographical variations in surface albedo, clouds, aerosols and vertical profiles of ozone.

[56] Such a comprehensive set of inputs has not been available for earlier retrievals of global surface UV radiation. We illustrate the impact of two of these inputs, aerosol type and cloud height, on UV irradiance. Figure 16a (Figure 16b) shows the surface UVB and Fu-Liou band 5 (UVA and Fu-Liou band 6) irradiances versus total column ozone at a SZA of 30° for clear conditions with a grassland albedo, and for the three distinct cases of OPAC continental clean (AOT of 0.05 at 550 nm), desert (AOT of 0.27) and urban (AOT of 0.26) aerosols (see Table 1). While desert and urban aerosols have nearly identical AOT in the visible, the strongly absorbing urban aerosol yields the same UVB at 290 DU as does the moderately absorbing desert aerosol at a much higher ozone loading of 400 DU (Figure 16a). The effect of aerosol absorption on band 5 irradiance is the same as on UVB irradiance. Hence both aerosol type and ozone loading are needed for an accurate estimate of UVB (band 5) with radiative transfer calculations. In contrast, while UVA (band 6) is little affected by ozone, aerosol forcing to UVA (band 6) remains significant (Figure 16b). Though aerosol type strongly affects the UVB and band 5 (UVA and band 6) irradiances, the ratio between UVB and band 5 (UVA and band 6) remains the same at various ozone concentrations and SZAs (that is why we can construct the R_{UVB} and R_{UVA} LUTs without considering aerosols).

[57] When the surface albedo is high, multiple reflections between cloud and ground can result in an appreciable absorption of UVB by tropospheric ozone. Figure 17 shows UVB irradiances versus column ozone at a SZA of 40° for a

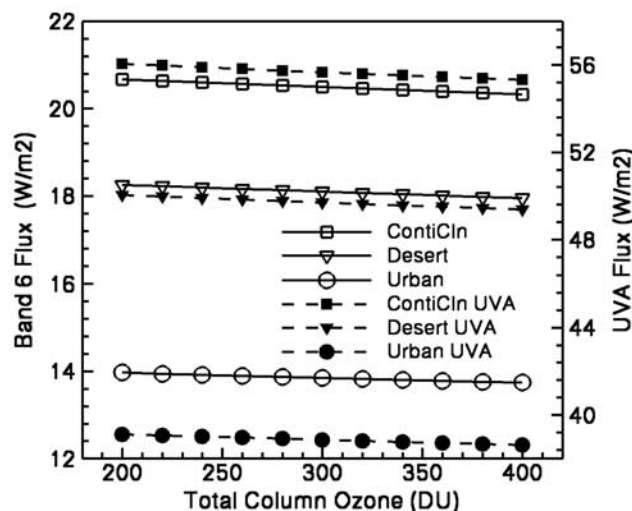


Figure 16b. Total surface downwelling band 6 (solid lines) and UVA (dashed lines) irradiances for different OPAC aerosols for midlatitude summer atmosphere, grassland surface, and solar zenith angle of 30° .

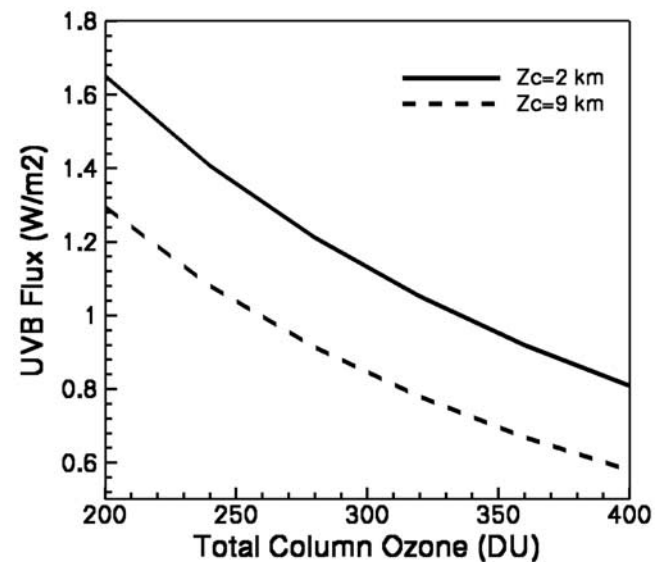


Figure 17. Surface UVB irradiances for Arctic winter atmosphere, maritime clean aerosols, snow surface, solar zenith angle of 40° , and cloud optical depth of 60, with effective cloud heights of 2 km (solid line) and 9 km (dashed line).

Table 3. Computed Downwelling UV at Surface as “True” (High-Resolution SBDART) and “LUT” (Parameterized Lookup Table)^a

	AOT = 0.0, COD = 0.0		AOT = 0.2, COD = 0.0		Aerosol Forcing	AOT = 0.2, COD = 10		Cloud Forcing
	Values	LUT Errors	Values	LUT Errors		Values	LUT Errors	
<i>SAZ = 0° and Surface Albedo Equals 0.0</i>								
True UVB	2.303	...	2.157	...	−0.146	1.345	...	−0.812
LUT UVB	2.309	−0.006	2.176	−0.019	−0.133	1.411	−0.066	−0.765
True UVA	66.03	...	63.13	...	−2.90	40.48	...	−22.65
LUT UVA	66.78	−0.75	63.88	−0.75	−2.90	41.67	−1.19	−22.21
True UV index	12.4	...	11.6	...		7.1	...	
LUT UV index	12.4	0.0	11.7	−0.1		7.4	−0.3	
<i>SAZ = 60° and Surface Albedo Equals 0.0</i>								
True UVB	0.425	...	0.382	...	−0.043	0.234	...	−0.148
LUT UVB	0.425	0.000	0.387	−0.005	−0.038	0.245	−0.011	−0.142
True UVA	26.94	...	24.49	...	−2.45	13.65	...	−10.84
LUT UVA	27.38	−0.44	25.22	−0.73	−2.16	14.39	−0.74	−10.83
True UV index	2.1	...	1.9	...		1.2	...	
LUT UV index	2.1	0	1.9	0.0		1.2	0.0	
<i>SAZ = 60° and Surface Albedo Equals 0.8</i>								
True UVB	0.606	...	0.550	...	−0.056	0.410	...	−0.140
LUT UVB	0.593	0.013	0.543	0.07	−0.050	0.435	−0.025	−0.108
True UVA	35.59	...	33.18	...	−2.41	25.64	...	−7.54
LUT UVA	36.04	−0.045	33.85	−0.67	−2.19	26.40	−0.76	−7.45
True UV index	3.0	...	2.7	...		2.1	...	
LUT UV index	3.0	0	2.7	0.0		2.2	−0.1	

^aValues for UVB (280–315 nm) in Wm^{-2} , UVA (315–400 nm) in Wm^{-2} , and UV index (erythral irradiance multiplied by 40) are given. Total column ozone of 300 DU, midlatitude summer atmosphere, and OPAC continental aerosol are assumed. Aerosol optical thickness (AOT) at 550 nm and cloud optical depth (COD) are noted.

snow surface and an Arctic winter atmospheric profile. The COD is 60 and cloud effective heights are 2 km (bottom at 1 km and top at 3 km) and 9 km (bottom at 8 km and top at 10 km) in this calculation. With the cloud at 2 km, the UVB is 0.8 Wm^{-2} at 400 DU. More tropospheric ozone is exposed to enhanced path lengths with the cloud at 9 km, and the UVB is then 0.8 Wm^{-2} only at a much reduced 310 DU.

[58] How well do the parameterized LUTs account for the scattering and absorption effects by the atmosphere and the surface? LUT errors (parameterized UV minus “true” UV from SBDART) are included in Table 3, which also serves as a quick reference for the effects of SZA, surface albedo, aerosols and cloudiness on UV at a fixed ozone loading (300 DU). The top matrix in Table 3 covers overhead sun for zero surface albedo and gives aerosol forcing (irradiance with aerosol minus irradiance without aerosol in clear skies) and cloud forcing (irradiance with clouds minus irradiance in clear skies); note the small value for UVB (2.3 Wm^{-2}) compared with UVA (66 Wm^{-2}) and the high UV index (12.4) for the case with no aerosols or clouds (left hand side). The UV index is released to the general public as integers up to 11; the value 12.4 would be released as 11+ and regarded as “extreme” by the US EPA. At overhead sun, the moderate AOT of 0.2 reduces the true UV index by almost 1 unit (from 12.4 to 11.6), but COD of 10 reduces the UV index to 7.1 (which is still regarded as “high”). LUT errors are considerably smaller than the aerosol forcing and cloud forcing, suggesting that application of the parameterization would yield suitable results.

[59] The middle matrix in Table 3 covers a SZA of 60° and surface albedo of zero. Values of UVA are reduced by more than a factor of 2 compared with SZA of 0° , and values of UVB and the UV index are reduced by roughly a factor of 6. All UV index values in the middle matrix are “low.” The lower matrix in Table 3 again covers SZA of

60° , but the surface albedo is increased to 0.8. Differences of the lower and middle matrices roughly indicate the forcing of snow albedo, which is here a unit increase in the UV index for each sky condition. Values for all UV parameters show little change from the pristine case of “no aerosols or clouds with zero surface albedo” (middle matrix on left) versus the opaque case of “clouds and aerosols with surface albedo 0.8” (lower matrix on right); while the cloud in the second case reflects much UV to space, the photons which do penetrate the cloud can experience multiple reflection from the snow, and this multiple reflection restores the downwelling UV radiation at the surface to its value in the pristine case. LUT errors for the UV index are again satisfactory. However, for high surface reflection, the error for clear UVB with AOT of 0.2 is comparable to the aerosol forcing (lower matrix near center), pointing to a limitation of the LUT. The effects of aerosol on surface UV are more pronounced at low SZA (upper matrix near center), where UV dosages are higher, and the LUT are more accurate.

7. Conclusion

[60] We developed lookup tables to relate CERES SARB outputs in the UV spectrum to surface UVB irradiance, UVA irradiance, and UV index. The sets of LUTs were used to convert irradiances of band 5 (298.5–322.5 nm) to UVB (280–315 nm) and band 6 (322.5–357.5 nm) to UVA (315–400 nm) separately for cloud-free and cloudy conditions for all surfaces. LUTs were also developed to convert retrieved UVB irradiance to UV index. The LUTs included the principal variables that affect the accuracy of retrieved UVB irradiance, UVA irradiance, and UV index. The accuracy of the retrieved surface UVB irradiance, UVA irradiance, and UV index were tested against the spectral

model integrated counterparts for 560 testing cases. The accuracies of the retrieved UVB and UVA irradiances are very good for both cloud-free and cloudy conditions with relative differences from -10% to 4% . The relative differences for the UV index are larger, -26% to 16% , because of error accumulation from two LUTs. The good agreements prove the LUTs that we developed work favorably well. In the future, the CERES SARB surface UV retrievals will be validated with ground measurements by UV networks and posted on line, just as SARB broadband retrievals are routinely compared with broadband surface networks (<http://www-cave.larc.nasa.gov/cave>).

[61] **Acknowledgments.** The authors would like to thank Gregory L. Schuster and William B. Grant for reading the manuscript and for their valuable comments. The authors also would like to express their appreciation to James Slusser and Gwen Scott for providing UV MFRSR data. Wenyng Su is supported by the CERES project under NASA grant NNL04AA26G.

References

- Arduini, R. F., P. Minnis, and D. F. Young (2002), Investigation of a visible reflectance parameterization for determining cloud properties in multi-layered clouds, paper presented at 11th Conference on Cloud Physics, Am. Meteorol. Soc., Ogden, Utah, 3–7 June.
- Bigelow, D. S., and J. R. Slusser (2000), Establishing the stability of multi-filter UV rotating shadow-band radiometers, *J. Geophys. Res.*, **105**, 4833–4840.
- Bigelow, D. S., J. R. Slusser, A. F. Beaubien, and J. H. Gibson (1998), The USDA ultraviolet radiation monitoring program, *Bull. Am. Meteorol. Soc.*, **79**, 601–615.
- Booth, G. E., T. B. Lucas, T. Mestechkina, J. R. Tusson IV, D. A. Neuschuler, and J. H. Morrow (1995), NSF Polar Programs UV spectroradiometer network 1993–1994 operating report, 203 pp., Biospherical Instrum., San Diego, Calif.
- Burrows, J. P., et al. (1999), The Global Ozone Monitoring Experiment (GOME): Mission concept and first scientific results, *J. Atmos. Sci.*, **56**, 151–175.
- Charlock, T. P., F. G. Rose, D. A. Rutan, T. L. Alberta, D. P. Kratz, L. H. Coleman, G. L. Smith, N. Manalo-Smith, and T. D. Bess (1997), Compute surface and atmospheric fluxes (System 5.0), CERES algorithm theoretical basis document, 84 pp., NASA Langley Res. Cent., Hampton, Va.
- Charlock, T. P., Z. Jin, F. G. Rose, K. Rutledge, W. L. Smith Jr., and D. A. Rutan (2002), The Surface and Atmospheric Radiation Budget and aerosol forcing with a new formulation for ocean surface albedo, paper presented at ARM Science Team Meeting, Atmos. Radiat. Meas. Program, St. Petersburg, Fla., 8–12 April.
- Coakley, J. A., Jr., W. R. Tahnk, A. Jayaraman, P. K. Quinn, C. Devaux, and D. Tanre (2002), Aerosol optical depths and direct radiative forcing for INDOEX derived from AVHRR: Theory, *J. Geophys. Res.*, **107**(D19), 8009, doi:10.1029/2000JD000182.
- Collins, W. D., P. J. Rasch, B. E. Eaton, B. V. Khattatov, J.-F. Lamarque, and C. S. Zender (2001), Simulating aerosols using a chemical transport model with assimilation of satellite aerosol retrievals: Methodology for INDOEX, *J. Geophys. Res.*, **106**, 7313–7336.
- d'Almeida, G. A., P. Koepke, and E. P. Shettle (Eds.) (1991), *Atmospheric Aerosols: Global Climatology and Radiative Characteristics*, 561 pp., A. Deepak, Hampton, Va.
- Dave, J. V. (1964), Meaning of successive iteration of the auxiliary equation in the theory of radiative transfer, *Astrophys. J.*, **140**, 1292–1303.
- Dave, J. V., and J. Gazdag (1970), A modified Fourier transform method for multiple scattering calculations in a plane parallel Mie atmosphere, *Appl. Opt.*, **9**, 1457–1466.
- Dubovik, O., and M. D. King (2000), A flexible inversion algorithm for retrieval of aerosol optical properties from Sun and sky radiance measurements, *J. Geophys. Res.*, **105**, 20,673–20,696.
- Eck, T. F., P. K. Bhartia, and J. B. Kerr (1995), Satellite estimation of spectral UVB irradiance using TOMS derived total ozone and UV reflectivity, *Geophys. Res. Lett.*, **22**, 611–614.
- Fu, Q., and K.-N. Liou (1993), Parameterization of the radiative properties of cirrus clouds, *J. Atmos. Sci.*, **50**, 2008–2025.
- Gao, W., J. R. Slusser, L. C. Harrison, P. Disterhoft, Q. Min, B. Olson, K. Lantz, and B. Davis (2001), Comparisons of UV synthetic spectra retrieved from the USDA UV multi-filter rotating shadow-band radiometer with collocated USDA reference UV spectroradiometer and NIWA UV spectroradiometer, *Proc. SPIE Int. Soc. Opt. Eng.*, **4482**, 408–414.
- Heath, D. F., A. J. Krueger, H. A. Roeder, and B. D. Henderson (1975), The Solar Backscatter Ultraviolet and Total Ozone Mapping Spectrometer (SBUV/TOMS) for Nimbus G, *Opt. Eng.*, **14**, 323–331.
- Herman, J. R., and E. A. Celarier (1997), Earth surface reflectivity climatology at 340–380 nm from TOMS data, *J. Geophys. Res.*, **102**, 28,003–28,011.
- Herman, J. R., P. K. Bhartia, J. Ziemke, Z. Ahma, and D. Larko (1996), UV-B radiation increase (1979–1992) from decreases in total ozone, *Geophys. Res. Lett.*, **23**, 2117–2120.
- Herman, J. R., P. K. Bhartia, O. Torres, C. Hsu, C. Seftor, and E. Celarier (1997), Global distribution of UV-absorbing aerosols from Nimbus-7/TOMS data, *J. Geophys. Res.*, **102**, 16,911–16,922.
- Herman, J. R., N. Krotkov, E. Celarier, D. Larko, and G. Labow (1999), Distribution of UV radiation at the Earth's surface from TOMS-measured UV-backscattered radiances, *J. Geophys. Res.*, **104**, 12,059–12,076.
- Hess, M., P. Koepke, and I. Schult (1998), Optical Properties of Aerosols and Clouds: The software package OPAC, *Bull. Am. Meteorol. Soc.*, **79**, 831–844.
- Holben, B. N., et al. (1998), AERONET: A federated instrument network and data archive for aerosol characterization, *Remote Sens. Environ.*, **66**, 1–16.
- Ignatov, A., and L. Stowe (2000), Physical basis, premises, and self-consistency checks of aerosol retrievals from TRMM VIRS, *J. Appl. Meteorol.*, **39**, 2259–2277.
- Jin, Z., T. P. Charlock, W. L. Smith Jr., and K. Rutledge (2004), A parameterization of ocean surface albedo, *Geophys. Res. Lett.*, **31**, L22301, doi:10.1029/2004GL021180.
- Joseph, J. H., W. J. Wiscombe, and J. A. Weinmann (1976), The delta-Eddington approximation for radiative flux transfer, *J. Atmos. Sci.*, **33**, 2453–2459.
- Kalliskota, S., J. Kaurola, P. Taalas, J. R. Herman, E. A. Celarier, and N. A. Krotkov (2000), Comparison of daily UV doses estimated from Nimbus 7/TOMS measurements and ground-based spectroradiometric data, *J. Geophys. Res.*, **105**, 5049–5058.
- Kaufman, Y. J., D. Tanre, L. A. Remer, E. F. Vermote, and A. Chu (1997a), Operational remote sensing of tropospheric aerosol over land from EOS moderate resolution imaging spectroradiometer, *J. Geophys. Res.*, **102**, 17,051–17,061.
- Kaufman, Y. J., D. Tanre, H. R. Gordon, T. Nakajima, J. Lenoble, R. Frouin, H. Grassl, B. M. Herman, M. D. King, and P. M. Teillet (1997b), Passive remote sensing of tropospheric aerosol and atmospheric correction for the aerosol effect, *J. Geophys. Res.*, **102**, 16,815–16,830.
- Kerr, J. B., and C. T. McElroy (1993), Evidence for large upward trends of ultraviolet-B radiation linked to ozone depletion, *Science*, **262**, 1032–1034.
- Krotkov, N. A., J. R. Herman, P. K. Bhartia, V. Fioletov, and Z. Ahmad (2001), Satellite estimation of spectral surface UV irradiance: 2. Effects of homogeneous clouds and snow, *J. Geophys. Res.*, **106**, 11,743–11,759.
- Long, C. N., and T. P. Ackerman (2000), Identification of clear skies from broadband pyranometer measurements and calculation of downwelling shortwave cloud effects, *J. Geophys. Res.*, **105**, 15,609–15,626.
- Lubin, D., E. H. Jensen, and H. P. Gies (1998), Global surface ultraviolet radiation climatology from TOMS and ERBE data, *J. Geophys. Res.*, **103**, 26,061–26,091.
- Mayer, B., C. A. Fischer, and S. Madronich (1998), Estimation of surface actinic flux from satellite (TOMS) ozone and cloud reflectivity measurements, *Geophys. Res. Lett.*, **25**, 4321–4324.
- McKinlay, A. F., and B. I. Diffey (1987), A reference action spectrum for ultraviolet induced erythema in human skin, *CIE J.*, **6**, 17–22.
- McPeters, R. D., T. Miles, L. E. Flynn, C. G. Wellemeyer, and J. M. Zawodny (1994), Comparison of SBUV and SAGE II ozone profiles: Implications for ozone trends, *J. Geophys. Res.*, **99**, 20,513–20,524.
- Minnis, P., D. F. Young, B. A. Wielicki, D. P. Kratz, P. W. Heck, S. Sun-Mack, Q. Z. Trepte, Y. Chen, S. L. Gibson, and R. R. Brown (2002), Seasonal and diurnal variations of cloud properties derived for CERES from VIRS and MODIS data, paper presented at 11th Conference on Atmospheric Radiation, Am. Meteorol. Soc., Ogden, Utah, 3–7 June.
- Mishchenko, M. I., I. V. Geogdzhayev, B. Cairns, W. B. Rossow, and A. L. Lacis (1999), Aerosol retrievals over the ocean by use of channels 1 and 2 AVHRR data: Sensitivity analysis and preliminary results, *Appl. Opt.*, **38**, 7325–7341.
- Molina, L. T., and M. J. Molina (1986), Absolute absorption cross sections of ozone in the 185 to 350 nm wavelength range, *J. Geophys. Res.*, **91**, 14,501–14,508.
- Platnick, S., J. Y. Li, M. D. King, H. Gerber, and P. V. Hobbs (2001), A solar reflectance method for retrieving cloud optical thickness and droplet size over snow and ice surfaces, *J. Geophys. Res.*, **106**, 15,185–15,199.

- Rabier, F., J.-N. Thepaut, and P. Courtier (1998), Extended assimilation and forecast experiments with a four-dimensional variational assimilation, *Q. J. R. Meteorol. Soc.*, **124**, 1861–1887.
- Ricchiazzi, P. S., Yang, C., Gautier, and D. Sowle (1998), SBDART: A research and teaching software tool for plane-parallel radiative transfer in the Earth's atmosphere, *Bull. Am. Meteorol. Soc.*, **79**, 2101–2114.
- Rose, F. G., and T. P. Charlock (1999), Profiles of longwave fluxes in clear skies using CERES data, ECWF data, and the Fu-Liou radiative transfer code, paper presented at 10th Conference on Atmospheric Radiation, Madison, Wisc., 28 June to 2 July.
- Rose, F., T. P. Charlock, D. Rutan, and G. L. Smith (1997), Tests of a constraint algorithm for the Surface and Atmospheric Radiation Budget, paper presented at 9th Conference on Atmospheric Radiation, Am. Meteorol. Soc., Long Beach, Calif., 2–7 Feb.
- Rossow, W. B., and R. A. Schiffer (1991), ISCCP cloud data products, *Bull. Am. Meteorol. Soc.*, **72**, 2–20.
- Rutan, D., and T. Charlock (1997), Spectral reflectance, directional reflectance, and broadband albedo of the Earth's surface, paper presented at 9th Conference on Atmospheric Radiation, Am. Meteorol. Soc., Long Beach, Calif., 2–7 Feb.
- Rutan, D., and T. Charlock (1999), Land surface albedo with CERES broadband observations, paper presented at 10th Conference on Atmospheric Radiation, Am. Meteorol. Soc., Madison, Wisc., 28 June to 2 July.
- Rutan, D., F. G. Rose, J. Madigan, and T. P. Charlock (2003), Surface albedo at the Atmospheric Radiation Measurement Southern Great Plains site from helicopter observations, paper presented at 13th ARM Science Team Meeting, Atmos. Radiat. Meas. Program, Broomfield, Colo., 31 March to 4 April.
- Schmid, B., P. R. Spyak, S. F. Bigar, C. Wehrli, J. Sekler, T. Ingold, C. Motzler, and N. Kompfer (1998), Evaluation of the applicability of solar and lamp radiometric calibrations of a precision Sun photometer operating between 300 and 1025 nm, *Appl. Opt.*, **37**, 3923–3941.
- Schuster, G. L., O. Dubovik, B. N. Holben, and E. E. Clothiaux (2005), Inferring black carbon content and specific absorption from Aerosol Robotic Network (AERONET) aerosol retrievals, *J. Geophys. Res.*, **110**, D10S17, doi:10.1029/2004JD004548.
- Shaw, G. E. (1976), Error analysis of multi-wavelength Sun photometry, *Pure Appl. Geophys.*, **114**, 1–14.
- Shettle, E. P. (1989), Models and aerosols, clouds and precipitation for atmospheric propagation studies, *AGARD Conf. Proc.*, **454**, 15–32.
- Slusser, J., G. Gibson, D. Bigelow, D. Kolinski, P. Disterhoft, K. Lantz, and A. Beaubien (2000), Langley method of calibrating UV filter radiometer, *J. Geophys. Res.*, **105**, 4841–4849.
- Tanre, D., L. A. Remer, Y. J. Kaufman, S. Mattoo, P. V. Hobbs, J. M. Livingston, P. B. Russell, and A. Smirnov (1999), Retrieval of aerosol optical thickness and size distribution over ocean from the MODIS airborne simulator during TARFOX, *J. Geophys. Res.*, **104**, 2261–2278.
- Tegen, I., and A. A. Lacis (1996), Modeling of particle size distribution and its influence on the radiative properties of mineral dust aerosol, *J. Geophys. Res.*, **101**, 19,237–19,244.
- Verdebot, J. (2000), A method to generate surface UV radiation maps over Europe using GOME, Meteosat, and ancillary geophysical data, *J. Geophys. Res.*, **105**, 5049–5058.
- Wielicki, B. A., B. R. Barkstrom, E. F. Harrison, R. B. Lee, G. L. Smith, and J. E. Cooper (1996), Clouds and the Earth's Radiant Energy System (CERES): An Earth Observing System experiment, *Bull. Am. Meteorol. Soc.*, **77**, 853–868.
- World Meteorological Organization (2003), Scientific assessment of ozone depletion: 2002, *Rep. 47*, 498 pp., Global Ozone Res. and Monit. Proj., Geneva.
- Yang, S.-K., S. Zhou, and A. J. Miller (1999), SMOBA: A 3-dimensional daily ozone analysis using SBUV/2 and TOVS measurement, Natl. Cent. for Environ. Predict., Camp Springs, Md.
- Young, D. F., P. Minnis, D. R. Doelling, G. G. Gibson, and T. Wong (1998), Temporal interpolation methods for the Clouds and the Earth's Radiant Energy System (CERES) experiment, *J. Appl. Meteorol.*, **37**, 572–590.

T. P. Charlock, NASA Langley Research Center, Hampton, VA 23681, USA.

F. G. Rose, Analytical Services and Materials, Inc., 107 Research Drive, Hampton, VA 23666-1340, USA.

W. Su, Center for Atmospheric Sciences, Hampton University, Hampton, VA 23668, USA. (w.su@larc.nasa.gov)